Arbitrary wavefront modulation utilizing an aperiodic elastic metasurface

Zhu-Long Xu, Dan-Feng Wang, Yun-Fei Shi, Zheng-Hua Qian, Badreddine Assouar, Kuo-Chih Chuang

Arbitrary wavefront modulation utilizing an aperiodic elastic metasurface

Zhu-Long Xu[1], Dan-Feng Wang[1], Yun-Fei Shi[1], Zheng-Hua Qian[2], Badreddine Assouar[3, a)], Kuo-Chih Chuang[1, a)]

[1]*Key Laboratory of Soft Machines and Smart Devices of Zhejiang Province, Institute of Applied Mechanics, School of Aeronautics and Astronautics, Zhejiang University, Hangzhou, 310027, China*

[2]*State Key Laboratory of Mechanics and Control of Mechanical Structures, College of Aerospace Engineering, Nanjing University of Aeronautics and Astronautics, Nanjing, 210016, China*

[3]*Institut Jean Lamour, CNRS, Universite de Lorraine, Nancy, 54506, France*

[a)] E-mail: badreddine.assouar@univ-lorraine.fr (Badreddine Assouar), chuangkc@zju.edu.cn (Kuo-Chih Chuang)

ABSTRACT

Metasurfaces have attracted much attention due to their much more compact configurations and their abilities to modulate wavefronts of propagating waves by abruptly shifting their phase and/or amplitude. Most current metasurfaces are usually composed of subunits with periodic unit cells, which limits their design freedom for arbitrary phase and amplitude modulation. To overcome this limitation, in this paper, we propose an aperiodic elastic metasurface where arbitrary phase and amplitude modulation can be achieved. The aperiodic elastic metasurface is composed of pillared resonators with different heights and an analytical model-based genetic algorithm (GA) inverse design method is employed to determine the heights of the pillared resonators. The proposed aperiodic elastic metasurface can steer and focus flexural waves with full transmission and can steer flexural waves into different directions with different amplitudes. The inverse design method and the aperiodic design in this paper can inspire the design of other types of functional metasurfaces for fascinating applications.

1. Introduction

Metasurfaces, pioneered in electromagnetics[1-6] and later extended to acoustics[7-12] and mechanics[13-17], are a class of subwavelength planar metamaterials which can modulate wavefronts of propagating waves by abruptly shifting their phase and/or amplitude. Metasurfaces that modulate the wavefronts by varying the phase distributions, referred to as phase gradient metasurfaces, have received extensive attention due to their easy designs, much more compact configurations, and multiple functionalities. The phase gradient metasurfaces are usually designed based on the generalized Snell's law (GSL), which links the phase gradient profile and the corresponding transmitted or reflected wave pattern[1, 8]. Most current metasurfaces can only cover a complete phase shift span (i.e., from 0 to 2π). However, to realize a full control of wavefronts (e.g., applications for holographic imaging[6, 18, 19] or particle manipulation[20, 21]), the subunit of the metasurface is required to also cover a normalized full amplitude shift span (i.e., from 0 to 1).

Since Zhu and Semperlotti[22] firstly realized anomalous refractions of elastic waves utilizing an elastic metasurface composed of locally resonant unit cells, different forms of elastic metasurfaces have been designed and various functionalities have been achieved. Jin *et al.* studied the resonant and scattering properties of the pillared resonators[23] and presented a compact metasurface consisting of a line of gradient pillared resonators for deep subwavelength focusing and imaging[24-26]. Cao *et al.*[27] proposed a flexural wave channel, composed of dual-layer elastic wave gradient metasurfaces, to achieve the asymmetrical flexural wave transmission. They also studied a disordered elastic metasurface composed of identical pillared resonators with a random arrangement. They found that the phase shifts and amplitudes of the subunits are only linearly related to the number of resonators and independent of the spatial arrangement of resonators within the decoupled region[28]. Zhang *et al.*[29] designed a metasurface to steer flexural waves, where the metasurface is constructed by an array of two-material composite beams with different length ratio. Recently, they further

proposed a metasurface with sinusoidally-shaped phononic beams to steer flexural waves by tuning the bending stiffness[30].

The above-mentioned elastic metasurfaces are all transmissive metasurfaces. Other than the transmissive metasurfaces, reflective metasurfaces have also been designed to achieve anomalous reflections. Based on gradient force-moment resonators, Xu *et al.*[31] proposed a deep-subwavelength metasurface, where each force-moment resonator is realized by stacking a lead block atop a silicone rubber block to steer and focus reflected flexural waves. Cao *et al*.[32] proposed a lossy metasurface utilizing strip-like plates, attached with a damping layer and a constrained layer, to realize a high-efficiency absorption of flexural waves. Ruan *et al.*[33] proposed a binary-cell elastic metasurface and realized the flexural-wave retroreflection by modulating the phase through changing the thickness of the cells. Instead of utilizing the GSL, they also designed a reflective elastic metasurface based on a surface impedance matched method.[34] Recently, Chuang *et al*.[35] proposed a tunable reflective elastic metasurface composed of zig-zag structures with different foldable angles. Apart from anomalous refraction and reflection, other functionalities and applications can be achieved by elastic metasurfaces such as wave mode conversion[15, 36, 37], wave mode splitting[38, 39], source illusion[40], and energy harvesting[13, 41-43].

Enhancing the efficiency of wavefront manipulation is one key issue in the design of metasurfaces[5, 44-46]. In acoustics, several designs and methods, including nonlocality[47, 48], bianisotropy[49, 50], and impedance matching[12, 51, 52] have been employed to realize high-efficiency metasurfaces. Several ways and structures have also been proposed to realize the high-efficiency elastic metasurfaces. Lee *et al.*[53] proposed a metasurface with spatially decomposable unit cells to independently tune the effective mass and stiffness and realize a full transmission of longitudinal waves by breaking the intrinsic proportional density-stiffness relation. Based on the phase accumulation, Cao *et al.*[54] proposed a pillared elastic metasurface that can support high transmissions of out-of-plane flexural waves. Also relying

on the phase accumulation, Jiang *et al*.[55] proposed a high-efficiency notched metasurface to manipulate flexural waves in which multiple parameters of the unit cells can be tuned independently. Rong *et al*.[56] proposed a multifunctional elastic metasurface with a high-energy transmission and robust manipulation utilizing a topology optimization. Since the GSL ignores the impedance-matching constraint, the above-mentioned GSL-based metasurfaces cannot redirect all the incident energy into a desired direction and this limits the efficiency of the elastic metasurface, especially at large deflection angles. Liu *et al*.[57] recently found the theoretical efficiency limits of anomalous refractions of the flexural waves based on the GSL and, by utilizing nonlocal coupling between the neighboring unit cells for impedance matching, they designed a high-efficiency elastic metasurface to break the GSL efficiency limit. Although such a design can realize wave deflecting with a high efficiency, the impedance matching method is difficult to expand to realize other complex functionalities such as wave focusing. On the other hand, although the full transmission of longitudinal waves has been studied, to the authors' knowledge, the full transmission of flexural waves on metasurfaces hasn't been realized. Since the manipulation of flexural waves are practical, it would be desirable to design a metasurface which can realize the full transmission of flexural waves.

In fact, full transmission of the flexural waves means that the transmitted waves have a unity nominal amplitude. In some cases, to achieve a certain goal, e.g., holography, a complete amplitude shift is also required in addition to the complete (i.e., 2π) phase shift. Since holography is one of the most important applications in optics and acoustics, several methods and structures have been proposed to design optical and acoustic metasurfaces where both phase and amplitude are modulated[11, 20, 58-61]. However, instead of amplitude, most existing elastic metasurfaces can only realize phase modulation. Liu *et al*.[62] designed an amplitude-shift elastic metasurface, composed of zigzag unit cells, to steer flexural waves. Also based on zigzag designs, Xu *et al*.[63] proposed a zigzag structure with a gradient index to simultaneously modulate the phase and amplitude. Wang *et al*.[64] realized the extreme

transmission of elastic zig-zag metasurface through the parametric optimization based on the genetic algorithm. Although the zigzag structure can realize both modulation of phase and amplitude shift and even the full transmission of waves, the fabrication of the zigzag structure might destroy the integrity of the host plate and thus sacrifice the strength and stiffness.

In this paper, based on an inverse design method, we propose an aperiodic elastic metasurface with simultaneous phase and amplitude modulation. Different from the previous periodic pillared elastic metasurface design, where all the pillared resonators within the subunit of which have identical height, the pillared resonators in our design are arranged aperiodically within the subunit. In addition, the heights of the pillared resonators are determined by a semi-analytical method based on a genetic algorithm. Compared with the general periodic elastic metasurface, much more abundant combinations between the phase and amplitude shifts, including full transmission of flexural waves, can be obtained. To illustrate the advantages of the aperiodic design, steering and focusing of flexural waves with full and controllable transmissions are later presented in this paper. Following the introduction, Section 2 presents the transmission characteristics for the subunit of the aperiodic pillared elastic metasurface. The aperiodic design of the elastic metasurface based on the GSL, including the steering and focusing of flexural waves, is described in Section 3 and Section 4, respectively. Experimental validations are also provided in Section 4. Finally, Section 5 presents the conclusions of this paper.

2. Transmission characteristics of the subunit of the aperiodic pillared elastic metasurface

Fig. 1 illustrates the general periodic and the proposed aperiodic design of the pillared elastic metasurface on a section of a plate. Here, to keep the integrity of the host plate, no slots are cut between adjacent subunits, despite the fact the presence of slots can minimize the coupling between the adjacent subunits. As shown in Fig. 1(a)-1(c), for the general design approach, pillared resonators are arranged periodically on the plate along the *x*-direction and

the pillared resonators with different heights are arranged along the *y*-direction to produce the desired phase gradient profile. However, for the aperiodic design approach as shown in Figs. 1(d)-1(f), the heights of the pillared resonators are different both in the *x*-direction and the *y*-direction. While it looks as being randomly arranged, we note that by carefully designing the heights of the pillared resonators within the subunit, desired transmission characteristics, including phase and amplitude of the transmitted waves in the subunit, might be obtained.

We have established an analytical plane strain model to obtain the transmission characteristics, including phase and amplitude of the transmitted waves, in the subunit on the pillared elastic metasurface. In this study, the subunit of the pillared elastic metasurface is composed of 8 pillared resonators. The subunit is divided into several regions, as shown in Fig. 2, and the *n*th unit cell of the subunit is composed of the *n*th host plate region (P_n), the (*n*+1)th host plate region (P_{n+1}) and the *n*th pillared resonator (R_n). As described in Ref[65], both longitudinal waves and flexural waves will simultaneously exist in the pillared elastic metasurface even if only flexural wave is excited to the host plate. Note that the longitudinal waves and flexural waves correspond to S0 and A0 lamb waves in the plate at low frequencies, respectively.

The governing equations for longitudinal waves and flexural waves in the host plates and the pillared resonators can be expressed in the following forms

$$\begin{aligned} &\frac{E_i}{\left(1-v_i^2\right)}\frac{\partial^2 u\left(x,t\right)}{\partial x^2}-\rho_i\frac{\partial^2 u\left(x,t\right)}{\partial t^2}=0 \\ &E_iI_i\frac{\partial^4 w\left(x,t\right)}{\partial x^4}+\rho_i d_i\frac{\partial^2 w\left(x,t\right)}{\partial t^2}=0 \end{aligned} \quad \left(i=\mathrm{P},\mathrm{R}\right), \tag{1}$$

where E, v, ρ, d and I are Young's modulus, Poisson's ratio, density, thickness and section moment of inertia, and $I_i=\dfrac{d_i^3}{12\left(1-v_i^2\right)}$. The subscript $i=\mathrm{P}$ represents the case of the host plates and $i=\mathrm{R}$ represents the case of the pillared resonators. The general solutions of

the transverse displacement $w(x,t)$ and longitudinal displacement $u(x,t)$ in Eq. (1) can be expressed in the following forms

$$\begin{aligned} u^{(j)} &= \left(A_1^{(j)} e^{-ik_{Li}x} + A_2^{(j)} e^{ik_{Li}x} \right) e^{i\omega t} \\ w^{(j)} &= \left(B_1^{(j)} e^{-ik_{Fi}x} + B_2^{(j)} e^{ik_{Fi}x} + B_3^{(j)} e^{-k_{Fi}x} + B_4^{(j)} e^{k_{Fi}x} \right) e^{i\omega t} \end{aligned} \quad (j = \mathrm{P}_1, \mathrm{P}_2, \ldots \mathrm{P}_9, \mathrm{R}_1, \mathrm{R}_2, \ldots \mathrm{R}_8), \tag{2}$$

where $k_{Li} = \sqrt{\dfrac{\rho_i \omega^2 \left(1 - \nu_i^2\right)}{E_i}}$ and $k_{Fi} = \left(\dfrac{\rho_i d_i \omega^2}{E_i I_i} \right)^{\frac{1}{4}}$ are the longitudinal wavenumber and flexural wavenumber, respectively, in which $\omega = 2\pi f$ is the circular frequency, $A_1^{(j)}$, $A_2^{(j)}$, $B_1^{(j)}$, $B_2^{(j)}$, $B_3^{(j)}$, $B_4^{(j)}$ are complex coefficients, $A_1^{(j)} e^{-ik_{Li}x}$ corresponds to the positive-going longitudinal waves and $A_2^{(j)} e^{ik_{Li}x}$ corresponds to the negative-going longitudinal waves, $B_1^{(j)} e^{-ik_{Fi}x}$ corresponds to the positive-going propagating flexural waves and $B_2^{(j)} e^{ik_{Fi}x}$ corresponds to the negative-going propagating flexural waves, and $B_3^{(j)} e^{-k_{Fi}x}$ corresponds to the positive-going evanescent flexural waves and $B_4^{(j)} e^{k_{Fi}x}$ corresponds to the negative-going evanescent flexural waves.

The physical quantities $u^{(\mathrm{P}_n)}$, $w^{(\mathrm{P}_n)}$, $\varphi^{(\mathrm{P}_n)}$, $F^{(\mathrm{P}_n)}$, $V^{(\mathrm{P}_n)}$, $M^{(\mathrm{P}_n)}$ and the complex coefficients $A_1^{(\mathrm{P}_n)}$, $A_2^{(\mathrm{P}_n)}$, $B_1^{(\mathrm{P}_n)}$, $B_2^{(\mathrm{P}_n)}$, $B_3^{(\mathrm{P}_n)}$, $B_4^{(\mathrm{P}_n)}$ in each plate region can be organized as a state vector $\boldsymbol{v}^{(\mathrm{P}_n)}$ and a coefficients vector $\boldsymbol{k}^{(\mathrm{P}_n)}$

$$\begin{aligned} \boldsymbol{v}^{(\mathrm{P}_n)} &= \left[u^{(\mathrm{P}_n)}, w^{(\mathrm{P}_n)}, \varphi^{(\mathrm{P}_n)}, F^{(\mathrm{P}_n)}, V^{(\mathrm{P}_n)}, M^{(\mathrm{P}_n)} \right] \\ \boldsymbol{k}^{(\mathrm{P}_n)} &= \left[A_1^{(\mathrm{P}_n)}, A_2^{(\mathrm{P}_n)}, B_1^{(\mathrm{P}_n)}, B_2^{(\mathrm{P}_n)}, B_3^{(\mathrm{P}_n)}, B_4^{(\mathrm{P}_n)} \right] \end{aligned} \quad (n = 1, 2, \ldots 9), \tag{3}$$

where φ, F, V and M are slope, axial force, shear force, and bending moment, respectively, and they can be expressed as

$$\begin{aligned} \varphi &= \frac{\partial w}{\partial x} \\ F &= \frac{Ed}{\left(1-v^2\right)}\frac{\partial u}{\partial x} \\ V &= -EI\frac{\partial^3 w}{\partial x^3} \\ M &= EI\frac{\partial^2 w}{\partial x^2} \end{aligned}. \tag{4}$$

For simplicity, the origin of coordinates is set at the interface among the P_n, P_{n+1} and R_n regions. Substitute Eqs. (2) and (4) into Eq. (3), we can relate state vector $\boldsymbol{v}^{(\mathrm{P}_n)}$ and coefficients vector $\boldsymbol{k}^{(\mathrm{P}_n)}$ in the following form

$$\boldsymbol{v}^{(\mathrm{P}_n)} = \boldsymbol{N}_1 \boldsymbol{k}^{(\mathrm{P}_n)} \quad \left(n = 1, 2, \ldots 9\right), \tag{5}$$

where $\boldsymbol{N}_1$ is the transformation matrix between the state vector and the coefficient vector at the same position, and the expression of $\boldsymbol{N}_1$ is presented in the supplementary material.

At the interfaces of the P_n, P_{n+1} and R_n regions, as shown in Fig. 2(b), the force in the *x* direction and *z* direction and the moment should be balanced at the connection position and the following boundary conditions must be satisfied,

$$\begin{aligned} &F^{(\mathrm{P}_n)} - F^{(\mathrm{P}_{n+1})} + V^{(\mathrm{R}_n)} = 0 \\ &V^{(\mathrm{P}_n)} - V^{(\mathrm{P}_{n+1})} - F^{(\mathrm{R}_n)} = 0 \qquad \left(n = 1, 2, \ldots 8\right). \\ &M^{(\mathrm{P}_n)} - M^{(\mathrm{P}_{n+1})} - M^{(\mathrm{R}_n)} = 0 \end{aligned} \tag{6}$$

The displacement in the *x* direction and *z* direction and the rotation angle are continuous at the connection position, so the following boundary conditions must be satisfied,

$$\begin{aligned} &u^{(\mathrm{P}_n)} = u^{(\mathrm{P}_{n+1})} \\ &u^{(\mathrm{P}_n)} = -w^{(\mathrm{R}_n)} \\ &w^{(\mathrm{P}_n)} = w^{(\mathrm{P}_{n+1})} \\ &w^{(\mathrm{P}_n)} = u^{(\mathrm{R}_n)} \qquad \left(n = 1, 2, \ldots 8\right). \\ &\varphi^{(\mathrm{P}_n)} = \varphi^{(\mathrm{P}_{n+1})} \\ &\varphi^{(\mathrm{P}_n)} = \varphi^{(\mathrm{R}_n)} \end{aligned} \tag{7}$$

The top end of the R_n region is free, hence the force in the *x* direction and *z* direction and the moment are 0,

$$\left.\begin{aligned} F^{(\mathrm{R}_n)}\big|_{z=h_{\mathrm{R}n}} &= 0 \\ V^{(\mathrm{R}_n)}\big|_{z=h_{\mathrm{R}n}} &= 0 \\ M^{(\mathrm{R}_n)}\big|_{z=h_{\mathrm{R}n}} &= 0 \end{aligned}\right. \quad (n=1, 2, \ldots 8). \tag{8}$$

Substitute Eq. (4) into Eqs. (6)-(8), we obtain

$$\boldsymbol{N}_2 \begin{bmatrix} \boldsymbol{k}^{(\mathrm{P}_{n+1})} \\ \boldsymbol{k}^{(\mathrm{R}_n)} \end{bmatrix} = \boldsymbol{N}_3 \boldsymbol{k}^{(\mathrm{P}_n)} \quad (n=1, 2, \ldots 8), \tag{9}$$

where $\boldsymbol{N}_2$ and $\boldsymbol{N}_3$ are 12×12 and 6×6 matrix respectively. The expression of $\boldsymbol{N}_2$ and $\boldsymbol{N}_3$ are presented in the supplementary material.

From Eq. (9), we can obtain

$$\begin{bmatrix} \boldsymbol{k}^{(\mathrm{P}_{n+1})} \\ \boldsymbol{k}^{(\mathrm{R}_n)} \end{bmatrix} = \boldsymbol{N}_2^{-1} \boldsymbol{N}_3 \boldsymbol{k}^{(\mathrm{P}_n)} = \boldsymbol{N}_4 \boldsymbol{k}^{(\mathrm{P}_n)} \quad (n=1, 2, \ldots 8). \tag{10}$$

From Eq. (10), we can obtain

$$\boldsymbol{k}_L^{(\mathrm{P}_{n+1})} = \boldsymbol{N}_5 \boldsymbol{k}_R^{(\mathrm{P}_n)} \quad (n=1, 2, \ldots 8), \tag{11}$$

where $\boldsymbol{k}_L^{(\mathrm{P}_{n+1})}$ indicates the coefficient vectors at the left end of the P_{n+1} region and $\boldsymbol{k}_R^{(\mathrm{P}_n)}$ indicates the coefficient vectors at the right end of the P_n region and $\boldsymbol{N}_5$ is the first to sixth rows of $\boldsymbol{N}_4$. For the P_n region with a length d, the relationship between the state vector at the right end and the coefficients vector at the left end can be expressed as

$$\boldsymbol{v}_R^{(\mathrm{P}_n)} = \boldsymbol{N}_6 \boldsymbol{k}_L^{(\mathrm{P}_n)} \quad (n=1, 2, \ldots 8), \tag{12}$$

and the expression of $\boldsymbol{N}_6$ is presented in the supplementary material. Here, the length of P_n region is composed of two parts, where one is the distance between the two pillared resonators d_s, and the other part is the effective thickness of the pillar resonators $\hat{d}$, thus $d = d_s + \hat{d} = d_s + d_r$.

From Eqs. (5), (11) and (12), the coefficients vector at the right end of the P_{n+1} region and

the coefficients vector at the right end of the region can be related by $\boldsymbol{N}_A^n$ as

$$\boldsymbol{k}_R^{(\mathrm{P}_{n+1})} = \boldsymbol{N}_1^{-1}\boldsymbol{v}_R^{(\mathrm{P}_{n+1})} = \boldsymbol{N}_1^{-1}\boldsymbol{N}_6\boldsymbol{k}_L^{(\mathrm{P}_{n+1})} = \boldsymbol{N}_1^{-1}\boldsymbol{N}_6\boldsymbol{N}_5\boldsymbol{k}_R^{(\mathrm{P}_n)} = \boldsymbol{N}_A^n\boldsymbol{k}_R^{(\mathrm{P}_n)} \quad (n=1,2,\ldots 8). \tag{13}$$

Then, we can obtain the coefficients vector at the right end of P_8 region as

$$\boldsymbol{k}_R^{(\mathrm{P}_8)} = \boldsymbol{N}_A^1\boldsymbol{N}_A^2\boldsymbol{N}_A^3\boldsymbol{N}_A^4\boldsymbol{N}_A^5\boldsymbol{N}_A^6\boldsymbol{N}_A^7\boldsymbol{k}_R^{(\mathrm{P}_1)}. \tag{14}$$

To obtain the phase and amplitude of the transmitted flexural waves, we need to obtain $\boldsymbol{k}_L^{(\mathrm{P}_9)}$, expressed as

$$\boldsymbol{k}_L^{(\mathrm{P}_9)} = \boldsymbol{N}_5\boldsymbol{k}_R^{(\mathrm{P}_8)} = \boldsymbol{N}_5\boldsymbol{N}_A^1\boldsymbol{N}_A^2\boldsymbol{N}_A^3\boldsymbol{N}_A^4\boldsymbol{N}_A^5\boldsymbol{N}_A^6\boldsymbol{N}_A^7\boldsymbol{k}_R^{(\mathrm{P}_1)}. \tag{15}$$

We consider the case when only the flexural wave is excited to the left end of the subunit. Thus, there will only be positive-going propagating flexural waves, negative-going propagating flexural waves, negative-going propagating longitudinal waves, and negative-going evanescent flexural waves in the P_1 region. Since the reflected waves in the right end of the subunit is not considered, there will only be positive-going propagating longitudinal waves, positive-going propagating flexural waves, and positive -going evanescent flexural waves in the P_9 region. Then, Eq. (15) can also be expressed as

$$\boldsymbol{k}_{Transmitted} = \boldsymbol{N}_5\boldsymbol{N}_A^1\boldsymbol{N}_A^2\boldsymbol{N}_A^3\boldsymbol{N}_A^4\boldsymbol{N}_A^5\boldsymbol{N}_A^6\boldsymbol{N}_A^7\boldsymbol{k}_{Incident}, \tag{16}$$

where $\boldsymbol{k}_{Incident} = \begin{bmatrix} 0 & r_L & 1 & r_F & 0 & r_F^* \end{bmatrix}^T$ and $\boldsymbol{k}_{Transmitted} = \begin{bmatrix} t_L & 0 & t_F & 0 & t_F^* & 0 \end{bmatrix}^T$. By solving Eq. (16), we can obtain t_F, and the phase ϕ and amplitude r of the transmitted flexural wave as

$$r = \mathrm{abs}\left(t_F\right) \tag{17}$$

and

$$\phi = \begin{cases} \arctan\left(\dfrac{\mathrm{Im}(t_F)}{\mathrm{Re}(t_F)}\right) + \pi + \dfrac{\pi}{2} & \text{if } Re(t_F) < 0 \\ \arctan\left(\dfrac{\mathrm{Im}(t_F)}{\mathrm{Re}(t_F)}\right) + \dfrac{\pi}{2} & \text{if } Re(t_F) > 0 \end{cases}. \tag{18}$$

We have first studied the transmission characteristics of the subunits on the periodic pillared elastic metasurface before designing the aperiodic one. Figs. 3(a) and 3(b) show the analytical phase and amplitude of the transmitted waves in the subunit of the periodic pillared elastic metasurface when the pillared resonators are with different heights, where the following design parameters are considered in calculation: the thickness of the host plate d_{P} is 1 mm, the thickness of the pillared resonator d_{R} is 1 mm, and the distance between the adjacent pillared resonators within a subunit d_s is 2 mm. The working frequency is chosen as 1000 Hz and the corresponding wavelength in the host plate is 98.9115 mm. The width of the subunit w_{P} is 0.2λ and the width of the pillared resonators w_{R} is $\frac{6}{7}w_{\mathrm{P}}$. The host plate is set as aluminum with a Young's modulus of 70 GPa, a Poisson's ratio of 0.33, and a density of 2700 kg/m^3. The pillared resonators are made of iron with a Young's modulus of 200 GPa, a Poisson's ratio of 0.30, and a density of 7870 kg/m^3. As a comparison, Figs. 3(c) and 3(d) show the phase and amplitude of the transmitted waves obtained from the finite element model (FEM) in COMSOL Multiphysics software. The correspondence of the phase and amplitude curves at different heights between the analytical model and FEM can be seen in Figs. 3(a) to 3(d). To have a better observation of the relationship between the analytical and simulation phases and amplitudes, in Fig. 3(e) we plot the phase and amplitude curves obtained from the analytical model (solid circle) and FEM (hollow diamond), where the corresponding pillared resonator heights are indicated with different colors. We can see that the two curves almost coincide with each other when the heights are small. However, as the height increases, there exists discrepancies between the two curves since the pillared resonators in the three-dimensional FEM are not in a plane strain state as those in the analytical one. We note that, if we consider

the phase and amplitude of the structure with only one pillared resonator, the curves obtained from the analytical model and the FEM can almost coincide with each other at all heights as shown in Fig. 3(f), indicating that although there are some differences between the analytical results and the simulation results, the difference is acceptable and we can determine the heights of the pillared resonators using the analytical model, and this argument will be validated later in this section.

It can be observed that the phase changes more rapidly with the height when the pillared resonators are high (more than 12 mm). To explain this phenomenon, the lowest dispersion bands of the unit cells with different heights, which is associated with the bending mode of the host plate, are plotted in Fig. 4(a). According to $c=\frac{2\pi f}{k}$, where c is the wave velocity, k is the wavenumber, and f is the frequency, at the same frequency, the change of wave velocity for two pillared resonators with different heights can be expressed as

$$\Delta c=\frac{2\pi f}{k_1}-\frac{2\pi f}{k_2}=2\pi f\frac{\Delta k}{k_1(k_1+\Delta k)}=\frac{2\pi f}{k_1}\frac{1}{1+\frac{k_1}{\Delta k}} \tag{19}$$

where Δc is the change of wave velocity, k_1, k_1 are wavenumbers for the two pillared resonators with different heights ($k_1, k_2>0$) and $\Delta k=k_2-k_1$ is the change of wavenumber. From Eq. (19), we can see that the change of wave velocity increases when the change of wavenumber increases. Fig. 4(a) shows that at a certain frequency (e.g., 1000 Hz), the change of wavenumber with respect to the height of the pillared resonator increases as the height of the pillared resonator increases, indicating that the change of wave velocity with respect to the height of the pillared resonator will also increase as the height of the pillared resonator increases. After propagating the same distance within the host plate, the flexural wave with different velocities will have different phase shifts, and the wave velocity of the flexural wave changes more rapidly with respect to the height when the pillared resonators are high, resulting in a more rapid change of the phase. To figure out the causes for the change of wave velocity,

as shown in Figs. 4(b) and 4(c), we plot the vibration modes of the pillared resonators with different heights. Figs. 4(b) and 4(c) show the z direction displacements in the pillared resonators associated with longitudinal vibration modes (longitudinal waves) and the x direction displacements in the pillared resonators associated with bending vibration modes (flexural waves), respectively. When the pillared resonators are short (less than 12 mm), the longitudinal vibration mode (longitudinal waves) is dominant in the pillared resonator. On the other hand, the bending vibration mode (the flexural wave) is dominant when the pillared resonators are high (more than 12 mm). When the propagating flexural wave in the plate encounters the pillared resonators, parts of them are converted into the longitudinal waves and the flexural waves in the pillared resonators, which will propagate in the pillared resonator and then back to the plate to interfere with the ongoing waves. This transmission process leads to a phase shift of the flexural waves in the host plate. In addition, the wave velocity of flexural wave is smaller than that of the longitudinal wave in the pillared resonators, and this explains the more rapid change of wave velocity in the host plate with respect to the height when the heights of the pillared resonators are high.

It can also be observed that the amplitude of the transmitted flexural wave oscillates between 0.2 and 1. The oscillation is caused by the Fabry Perot resonance[40]. This can be demonstrated by comparing the phases at the peak points of the amplitude curve. As shown in Fig. 5, we plot the amplitude curves of the subunits with different pillared resonators. It can be observed that within the same height range, amplitude curves of the subunits with more pillared resonators have more peaks and the phases at the peak points of the amplitude curves are either 3.5 or 0.4 rad, meaning that the difference of the phase between these peak points are approximate π. Fabry Perot resonance between two cylinder-pillared resonators has been studied in Ref[66], in which the resonance frequencies of the compressional mode of the two cylinder-pillared resonators are within the working frequency range and Fabry Perot resonance happens when the distance between the two cylinder-pillared resonators is half of the

wavelength. However, in our design, the working frequency is much smaller than the resonance frequency of the compressional mode of the pillared resonators and the bending mode is dominated within the Fabry Perot resonance region, and thus the Fabry Perot resonance is related to the height of the pillared resonators. It should be noted that the Fabry Perot resonance has been utilized to enhance the efficiency of sensors and actuators in elastic waves. Here, we can see that due to the Fabry Perot resonance, high transmission of flexural waves can be achieved.

In a general periodic metasurface design, the pillared resonators within one subunit have identical height. As shown in Fig. 3(e), the amplitude can correspond to only one or two values at a given phase. At some phases, the amplitude of the transmitted waves is only about 60% of the full transmission, which will greatly reduce the efficiency of the metasurface when using these subunits to construct the metasurface. To account for the cause of the low transmission, we plot the amplitude of the transmitted flexural wave, reflected flexural wave, transmitted longitudinal wave, and reflected longitudinal wave as shown in Fig. 6(a). We can see that the amplitudes of the transmitted and reflected longitudinal waves are rather small compared with that of the transmitted and reflected flexural waves. It means that although both the flexural and longitudinal wave are considered in the analytical model, the longitudinal wave can be ignored in the designing process. In fact, the low transmission is caused by the mismatch of the impedance. Specifically, the phase shift is realized by the change of the phase speed, which is proportional to $\sqrt{K_{eff} / M_{eff}}$, while the amplitude is determined by the impedance of the pillared resonators, which is proportional to $\sqrt{K_{eff} M_{eff}}$,where K_{eff} refers to the effective stiffness and M_{eff} refers to the effective mass[53]. For the design of the periodic metasurface, all the heights of the pillared resonators are the same and thus there is only one design freedom that can be taken into consideration. Then, combination possibilities between the effective mass and stiffness are limited and thus one can only moderately modulate the phase and amplitude

utilizing a periodic metasurface. However, for an aperiodic design, where the pillared resonators within one subunit can have different heights, much richer combinations between the effective mass and stiffness can be achieved which might enable more accurate and abundant phase and amplitude modulation of the wavefronts.

To verify the concept of using the aperiodic design for an abundant wavefront modulation, we first consider the design of an aperiodic subunit where the height of only one pillared resonator is different from other pillared resonators. The phase and amplitude of the transmitted waves when the pillared resonator with different height is located at different positions is shown in Figs. 7(a)-7(d) and the combination range between phase and amplitude with only one different pillared resonator is shown in Fig. 7(e). We can see that, in addition to the height, the position of the pillared resonator with different height will also influence the phase and amplitude of the transmitted waves. Due to the symmetry configuration of the metasurface, the results of the other four arrangements (i.e., the resonator with different height is located at the position of the 5th, 6th, 7th, or 8th location) are the same as the four ones presented in Fig. 7. We can see that, although only one of the pillared resonators is designed to have different height, phase and amplitude can cover a much wider range. Then, one can obviously expect, if all the eight pillared resonators have different heights, much more abundant modulations between the phase and amplitude can be achieved and accordingly more precise and complete modulation of the wavefronts can be achieved.

However, different from the periodic design, where one can easily determine the pillar height to obtain the desired phase, it is difficult to determine the heights of each pillared resonator to obtain the desired transmission characteristics in the aperiodic design. Luckily, the design of the height of the pillared resonators on the aperiodic metasurface can be treated as an optimization problem and here the genetic algorithm (GA)[67-71] is employed to find the optimized heights of each subunit. To determine the heights, we firstly find out the optimized heights based on the analytical model. Then, based on the analytical heights, we determine the

corresponding heights using the FEM results to minimize the design error presented in the ideal analytical model. Due to the nature of the genetic algorithm[72], it should be noted that the solution to the optimization problem is not unique but the results can support the concept of achieving much more abundant combinations between the phase and amplitude, including the full transmission of flexural waves, using the aperiodic metasurface. The genetic algorithm (GA) is a method to solve optimization problems based on natural selection, a process that drives the biological evolution. The first step of GA is to create an initial population with a size p_0 and the generation of initial population is random. The individuals in the population are the possible solutions to the optimization problem, i.e., the heights of the eight pillared resonators within one subunit in this paper. Then, based on the fitness value of each individual in the initial population, which can be obtained from a fitness function, GA will select some individuals as parents, and these parents will generate the next generation, and the individuals in the next generation are called children. The next generation is composed of three kinds of children, including elite children, crossover children and mutation children. Elite children are the individuals in the current population with the best fitness values. These individuals automatically survive to the next population without any change and the number of elite children is ap_0. Crossover children are created by combining the vectors of a pair of parents and the number of crossover children is $(1-a)bp_0$. The rest are mutation children that are created by introducing random changes, or mutations, to a single parent. The process described above is one optimization round and this optimization round is repeated until the average change in the fitness value is less than the specificized value. In this paper, the GA toolbox embedded in MATLAB is utilized to solve the optimization problem and, by default, a=0.05, b=0.8. The objective function in this paper is defined as the summation of the difference between optimized amplitudes and target amplitudes and the difference between optimized phases and target phases as

$$\begin{aligned} &\min F(x) = \alpha\left|r_t - r_o\right| + \beta\left|\varphi_t - \varphi_o\right| \quad x = \left(h_{\mathrm{R1}}, h_{\mathrm{R2}}, h_{\mathrm{R3}}, h_{\mathrm{R4}}, h_{\mathrm{R5}}, h_{\mathrm{R6}}, h_{\mathrm{R7}}, h_{\mathrm{R8}}\right) \\ &\text{s.t.} \quad h_{\min} \le h_{\mathrm{R1}}, h_{\mathrm{R2}}, h_{\mathrm{R3}}, h_{\mathrm{R4}}, h_{\mathrm{R5}}, h_{\mathrm{R6}}, h_{\mathrm{R7}}, h_{\mathrm{R8}} \le h_{\max}, \end{aligned} \tag{20}$$

where r_t and φ_t are target amplitude and phase, r_o and φ_o are optimized amplitude and phase, α and β are weighting parameters and we choose $\alpha = 1$ and $\beta = 2\pi$.

To demonstrate that the aperiodic metasurface can realize arbitrary phase and amplitude modulation of the wavefronts, we plot different combinations of phases and amplitudes obtained from the aperiodic design with a phase interval of 0.5 rad and an amplitude interval of 0.2 as shown in Fig. 8(a). The blue circles represent the analytical results and the red triangles represent the corresponding FEM results. Due to the differences between the ideal plane strain theoretical model and the three-dimensional FEM one, there will exist some discrepancies between the analytical results and the simulation ones. While one can design pillared resonators directly in COMSOL with its built-in optimization module[73-75] to obtain more precise phase and amplitude, the proposed analytical model-based genetic algorithm design approach is much more efficient. As shown in Figs. 8(b) and 8(c), we plot the out-of-plane displacement distribution of the transmitted wave field in the subunit with the same phase (1 rad) but different amplitudes (an interval of 0.2) and the same amplitude (1) but different phases (an interval of 1 rad), respectively, where the left numbers indicate the phases and the right numbers indicate the amplitudes obtained from FEM, respectively. We can see that based on our aperiodic design, in addition to the phase, the amplitude of the transmitted waves can also be modulated simultaneously. As a comparison, we also plot the out-of-plane displacement distribution in the subunit with the same phases for the periodic design as shown in Fig. 8(d). Compared with the results shown in Fig. 8(c), we can clearly see that to some phases, the amplitude of the transmitted waves is very low, while the normalized amplitude is almost 1 in the aperiodic design. From the above analysis, we can see that much more combinations between phases and amplitudes, including full transmission of flexural waves, can be realized based on the

aperiodic design.

To understand the mechanism of the full transmission, as shown in Fig. 9, we plot the amplitude and phase at different frequencies of the subunit of the periodic and aperiodic metasurface. It can be observed that the full transmission corresponds to the peak of the Fabry Perot resonance region, and different from the periodic design, in which the peak of the Fabry Perot region is narrow and single, for the aperiodic one the region is wide and multiple. This phenomenon, caused by the coupling between different Fabry Perot cavities, can also be observed in multilayer partially reflective surfaces[76]. In the aperiodic design, pillared resonators with different heights can be regard as Fabry Perot cavities with different peaking frequencies, and by combining them together, the coupling between theses pillared resonators can broaden the high-transmission region.

3. Steering flexural waves utilizing the aperiodic pillared elastic metasurface

In this and the following sections, we use steering and focusing of flexural waves as two demonstration examples to illustrate the advantages of the aperiodic elastic metasurface on realizing arbitrary wavefront modulation of the flexural waves. We first design an aperiodic elastic metasurface to steer flexural waves. When designing the elastic metasurface to steer flexural waves, gradient phase shifts along the *y*-direction (as shown in Fig. 1) is necessary and the theoretical refraction angle θ_t of the transmitted waves can be obtained by the GSL as

$$\theta_t = \arcsin(\sin\theta_i + \frac{\lambda}{2\pi}\frac{d\phi}{dy}) \tag{21}$$

where θ_i is the incident angle and $\frac{d\phi}{dy}$ is the spatial phase shift gradient. Here, a vertical incident flexural wave (i.e., $\theta_i = 0$) is considered and two cases of flexural wave steering are presented in this section. The first case is to illustrate that the aperiodic metasurface can realize the full transmission of flexural waves and the second case is to illustrate that the aperiodic

metasurface can realize the amplitude modulation that is potential in providing more abundant wave manipulations. In the first case, we steer the vertical incident flexural waves into only one direction, where the phase shift $d\phi$ between the adjacent subunit is $\frac{\pi}{12}$, the spatial phase shift gradient $\frac{d\phi}{dy}=\frac{\pi/12}{0.2\lambda}=13.23$ and the refraction angle $\theta_t=12.02^\circ$. The subunit without the presence of the pillared resonators can be regarded as a reference subunit #1, and another 23 subunits with pillared resonators are arranged to produce the desired phase shifts. Figs. 10(a) and 10(b) show the theoretical desired phase shifts and the phase shifts obtained from the 3D FEM of the periodic design and the aperiodic design, respectively. We can see that the average transmission of these subunits is about 0.88 and the two designs can both achieve the desired phase shifts but the amplitude at some phase shifts is rather low for the periodic design, which will influence the steering efficiency. However, the aperiodic design can not only achieve the desired phase shifts, but can also achieve the nearly-full transmission for all the subunits and the average transmission of the subunits is about 0.99. The corresponding out-of-plane displacement distributions in the transmitted wave field of the subunits are plotted in Fig. 11(a), where only 12 subunits with phase interval as $\frac{\pi}{6}$, instead of all large number of subunits, are plotted for clarity. We can clearly see that the subunits can obtain the desired phase shifts and can realize almost full transmissions of the flexural waves.

After analyzing the transmission characteristics for the subunits, we assemble these subunits to steer flexural waves. The out-of-plane displacement distribution in the incident wave field and the transmitted wave field are plotted as shown in Fig. 12(a). It can be clearly observed that the vertically incident flexural waves have been deflected by the designed aperiodic elastic metasurface. In order to obtain the refraction angle from the numerical simulations, the polar directivity graph of the transmitted waves measured at three wavelengths away from the center of the metasurface is shown in Fig. 12(b). It can be observed that the

refraction angle is 10.64°, which has a good agreement with the theoretical one. In addition, utilizing the same subunits but with a spatial phase shift gradient $\frac{d\phi}{dy}=\frac{\pi/6}{0.2\lambda}=26.46$, we steer the flexural waves into another direction with a refraction angle $\theta_t=24.62^{\circ}$. The corresponding out-of-plane displacement distribution in the incident wave field and the transmitted wave field of this case are plotted in Fig. 12(c) and the polar directivity graph of the transmitted waves measured at three wavelengths away from the center of the metasurface is shown in Fig. 12(d). The refraction angle is 27.32°, which also has a good agreement with the theoretical one.

Next, the aperiodic metasurface is exploited to steer the flexural waves into different directions with different amplitudes and we note that this function cannot be realized by the general periodic metasurface. The theoretical desired phase and amplitude distribution, together with the phase and amplitude distribution obtained from the 3D FEM of the aperiodic design along the metasurface, are shown in Fig. 13(a). The numerical results of the out-of-plane displacement distribution in the incident wave field and the transmitted wave fields and the polar directivity graph of the transmitted waves measured at three wavelengths away from the center of the metasurface are plotted in Figs. 13(b) and 13(c), respectively. We can clearly see that the incident waves have been deflected into two different directions and the amplitudes of the two direction transmitted waves are different amplitudes. Although there are some discrepancies between the numerical and theoretical refraction angles of the two directions probably due to the coupling between the subunits emerging from the amplitude difference among the subunit plate, the ability to split flexural wave with different amplitudes have been demonstrated.

4. Focusing flexural waves utilizing the aperiodic pillared elastic metasurface

Apart from steering waves, the aperiodic pillared elastic metasurface can also focus flexural waves. Focusing waves requires a hyperbolic phase profile satisfying

$$\phi(y) = \frac{2\pi}{\lambda}(\sqrt{F^2 + y^2} - F), \tag{22}$$

where y is the coordinate along the metasurface as shown in Fig. 1 ($y = 0$ is on the axis of the symmetry) and F is the designed focal distance, chosen as 3λ in this paper.

Figs. 14(a) and 14(b) show the amplitude and phase of the subunits to focus flexural wave designed based on the aperiodic design and periodic design, respectively. It can be observed that the two designs can both achieve the desired phase profile, but the amplitude at some phase is rather low for the periodic design, and the average transmission of these subunits in the periodic design is about 0.88, which will influence the focusing efficiency. However, we can see that the aperiodic design not only can achieve the desired phase profile, but can also achieve a nearly-full transmission for all the subunits, where the average transmission of the subunits is about 0.99.

After analyzing the transmission characteristics of the subunits, we assemble these subunits to form a metasurface and study its wave focusing effect. The simulated displacement and energy distribution in the transmitted wave field are shown in Figs. 15(a) and 15(b), respectively. We can clearly see a focal area appears after the incident wave passes through the elastic metasurface and the focal distance is approximately about 3λ. To further demonstrate that the aperiodic design can improve the efficiency of wave focusing, we plot the energy intensity of the periodic design and aperiodic design as shown in Figs. 15(c) and 15(d). The peak normalized intensity of the periodic design is about 5.549, while the peak normalized intensity of the aperiodic design is about 6.623 and the focusing efficiency has increased about 19.35%.

We then set up an experiment to verify the simulation focusing results and the feasibility

of the aperiodic design of metasurfaces. In the above sections, we choose the material of the host plate as aluminum and the material of the pillared resonators as iron, and the working frequency is chosen as 1000 Hz to better illustrate the advantages (e.g., high efficiency of focusing) of the aperiodic design. In the experiment, for the convenience of fabrication, the host plate and the pillared resonators both have the same material as aluminum and the working frequency is chosen as 8000 Hz. Utilizing the same method in the above sections, we redesign the aperiodic elastic metasurface to focus waves and the details of this design is illustrated in the supplementary material.

The photo of the experimental setup is shown in Fig. 16. The aperiodic metasurface and the host plate were fabricated from a same aluminum plate through a milling technology. As mentioned in Section 2, no slots are cut between adjacent subunits and thus the integrity of the host plate are indeed kept. An array composed of seven piezoelectric sheets was bonded on the surface of the host plate to generate the A0 Lamb waves. A layer of blue-tack was attached to the boundary to minimize reflections from the boundary of the plate. An 8 kHz 5-count Hanning-windowed tone burst was generated by a signal generator and the signal was sent to the power amplifier, which drives the piezoelectric sheets. A scanning Laser Doppler Vibrometer (LDV) system (Polytec PSV-500) was utilized to measure the out-of-plane propagating velocity of the host plate. The LDV system has a built-in bandpass filter from 7 kHz to 9 kHz. To avoid the environmental disturbances, the response at each location is measured three times and averaged before the LDV scans the next location. The sample frequency is 100 kHz and the time resolution is $5\mu s$. One flexural wavelength contains about 15 scanning points in this experiment.

The experimental distributions of the out-of-plane velocity at the incident end and transmitted end are shown in Fig. 17. As a comparison, the results obtained from the simulation are also presented. It can be observed that plane incident flexural wave will focus in the transmitted end, where the velocity at the focal distance is much larger than that in the incident

end, and the focal distance is about 3λ. The experimental results agree well with the simulation results, demonstrating the accuracy of the simulation results and the feasibility of the aperiodic metasurface.

5. Conclusions

In this paper, we have proposed an aperiodic elastic metasurface consisting of pillared resonators that can realize arbitrary phase and amplitude modulation of the wavefronts. Different from the general periodic metasurface, where the subunits are composed of identical unit cells, the subunits of the aperiodic metasurface are composed of different unit cells, where the heights of the pillared resonators within the subunit can be determined by an analytical model-based genetic algorithm inverse design method. The proposed aperiodic elastic metasurface can steer and focus flexural waves with almost full transmission. Utilizing the aperiodic design, the focusing efficiency can be increased by 19.35%, compared with that of the general periodic design. In addition, the proposed aperiodic elastic metasurface can steer waves into different directions with different amplitudes, which cannot be realized by the general periodic metasurface. The proposed aperiodic metasurface and its inverse design method can inspire the design of other types of metasurfaces, and open a promising route for applications such as on energy harvesting or holographic imaging.

CRediT authorship contribution statement

Zhu-Long Xu: Conceptualization, Investigation, Methodology, Validation, Writing - original draft. **Dan-Feng Wang:** Validation, Methodology. **Yun-Fei Shi:** Validation, Methodology. **Zheng-Hua Qian:** Writing – review and editing, Funding acquisition. **Badreddine Assouar:** Writing – review and editing. **Kuo-Chih Chuang:** Project administration, Writing – review and editing, Funding acquisition.

Declaration of Competing Interest

The authors declare that they have no known competing financial interests or personal relationships that could have appeared to influence the work reported in this paper.

Acknowledgments

Financial support by the National Natural Science Foundation of China (Grant No. 11972318) and State Key Laboratory of Mechanics and Control of Mechanical Structures (Nanjing University of Aeronautics and Astronautics, Grant No. MCMS-E-0521G01) are gratefully acknowledged.

References

[1] Yu N, Genevet P, Kats MA, Aieta F, Tetienne J-P, Capasso F, et al. Light propagation with phase discontinuities: Generalized laws of reflection and refraction. Science 2011;334:333-337.

[2] Ni X, Emani NK, Kildishev AV, Boltasseva A, Shalaev VM. Broadband light bending with plasmonic nanoantennas. Science 2012;335:427-427.

[3] Ni X, Kildishev AV, Shalaev VM. Metasurface holograms for visible light. Nat Commun 2013;4:1-6.

[4] Lin D, Fan P, Hasman E, Brongersma ML. Dielectric gradient metasurface optical elements. Science 2014;345:298-302.

[5] Abdollahramezani S, Hemmatyar O, Taghinejad M, Taghinejad H, Krasnok A, Eftekhar AA, et al. Electrically driven reprogrammable phase-change metasurface reaching 80% efficiency. Nat. Commun. 2022;13:1-11.

[6] Deng Z-L, Li G. Metasurface optical holography. Mater Today Phys 2017;3:16-32.

[7] Zhu Y, Fan X, Liang B, Cheng J, Jing Y. Ultrathin acoustic metasurface-based schroeder diffuser. Phys Rev X 2017;7:021034.

[8] Xie Y, Wang W, Chen H, Konneker A, Popa B-I, Cummer SA. Wavefront modulation and subwavelength diffractive acoustics with an acoustic metasurface. Nat Commun 2014;5:1-5.

[9] Zhu Y, Merkel A, Donda K, Fan S, Cao L, Assouar B. Nonlocal acoustic metasurface for ultrabroadband sound absorption. Phys Rev B 2021;103:064102.

[10] Wang X, Fang X, Mao D, Jing Y, Li Y. Extremely asymmetrical acoustic metasurface mirror at the exceptional point. Phys Rev Lett 2019;123:214302.

[11] Li P, Du Q, Xu Z, Xu Y, Wang Q, Peng P. Stepped acoustic metasurface with

simultaneous modulations of phase and amplitude. Appl Phys Express 2021;14:127001.
[12] Ma G, Yang M, Xiao S, Yang Z, Sheng P. Acoustic metasurface with hybrid resonances. Nat Mater 2014;13:873-878.
[13] De Ponti JM, Colombi A, Ardito R, Braghin F, Corigliano A, Craster RV. Graded elastic metasurface for enhanced energy harvesting. New J Phys 2020;22:013013.
[14] Chen A-L, Wang Y-S, Wang Y-F, Zhou H-T, Yuan S-M. Design of acoustic/elastic phase gradient metasurfaces: Principles, functional elements, tunability, and coding. Appl Mech Rev 2022;74:020801.
[15] Lee SW, Seung HM, Choi W, Kim M, Oh JH. Broad-angle refractive transmodal elastic metasurface. Appl Phys Lett 2020;117:213502.
[16] Yaw Z, Zhou W, Chen Z, Lim C. Stiffness tuning of a functional-switchable active coding elastic metasurface. Int J Mech Sci 2021;207:106654.
[17] Shen X, Sun C-T, Barnhart MV, Huang G. Elastic wave manipulation by using a phase-controlling meta-layer. J Appl Phys 2018;123:091708.
[18] Huang L, Zhang S, Zentgraf T. Metasurface holography: From fundamentals to applications. Nanophotonics 2018;7:1169-1190.
[19] Tian Y, Wei Q, Cheng Y, Liu X. Acoustic holography based on composite metasurface with decoupled modulation of phase and amplitude. Appl Phys Lett 2017;110:191901.
[20] Zheng C, Li J, Yue Z, Li J, Liu J, Wang G, et al. All-dielectric trifunctional metasurface capable of independent amplitude and phase modulation. Laser Photonics Rev 2022;2200051.
[21] Zhu Y, Hu J, Fan X, Yang J, Liang B, Zhu X, et al. Fine manipulation of sound via lossy metamaterials with independent and arbitrary reflection amplitude and phase. Nat Commun 2018;9:1-9.
[22] Zhu H, Semperlotti F. Anomalous refraction of acoustic guided waves in solids with geometrically tapered metasurfaces. Phys Rev Lett 2016;117:034302.
[23] Jin Y, Bonello B, Moiseyenko RP, Pennec Y, Boyko O, Djafari-Rouhani B. Pillar-type acoustic metasurface. Phys Rev B 2017;96:104311.
[24] Jin Y, Wang W, Khelif A, Djafari-Rouhani B. Elastic metasurfaces for deep and robust subwavelength focusing and imaging. Phys Rev Appl 2021;15:024005.
[25] Wang W, Iglesias J, Jin Y, Djafari-Rouhani B, Khelif A. Experimental realization of a pillared metasurface for flexural wave focusing. APL Mater 2021;9:051125.
[26] Jin Y, Pennec Y, Bonello B, Honarvar H, Dobrzynski L, Djafari-Rouhani B, et al. Physics of surface vibrational resonances: Pillared phononic crystals, metamaterials, and metasurfaces. Reports on progress in physics 2021;84:086502.
[27] Cao L, Xu Y, Assouar B, Yang Z. Asymmetric flexural wave transmission based on dual-layer elastic gradient metasurfaces. Appl Phys Lett 2018;113:183506.
[28] Cao L, Yang Z, Xu Y, Fan S-W, Zhu Y, Chen Z, et al. Disordered elastic metasurfaces. Phys Rev Appl 2020;13:014054.

[29] Zhang J, Su X, Liu Y, Zhao Y, Jing Y, Hu N. Metasurface constituted by thin composite beams to steer flexural waves in thin plates. Int J Solids Struct 2019;162:14-20.
[30] Zhang X, Zhang J, Hu N, Zhang C. A subwavelength sinusoidally-shaped phononic beam structures-based metasurface for flexural wave steering. Appl Acoust 2022;194:108790.
[31] Zhao T, Yang Z, Tian W, Cao L, Xu Y. Deep-subwavelength elastic metasurface with force-moment resonators for abnormally reflecting flexural waves. Int J Mech Sci 2022;221:107193.
[32] Cao L, Yang Z, Xu Y, Fan S-W, Zhu Y, Chen Z, et al. Flexural wave absorption by lossy gradient elastic metasurface. J Mech Phys Solids 2020;143:104052.
[33] Ruan Y, Liang X, Hu C. Retroreflection of flexural wave by using elastic metasurface. J Appl Phys 2020;128:045116.
[34] Ruan Y, Liang X. Reflective elastic metasurface for flexural wave based on surface impedance model. Int J Mech Sci 2021;212:106859.
[35] Xu Z-L, Yu S-B, Liu J, Chuang K-C. A tunable zig-zag reflective elastic metasurface. Crystals 2022;12:1170.
[36] Kim MS, Lee WR, Kim YY, Oh JH. Transmodal elastic metasurface for broad angle total mode conversion. Appl Phys Lett 2018;112:241905.
[37] Yaw Z, Lim C, Zhong Z, Zhou W. High efficiency generation of s-wave via a transmissive binary coding metasurface based on machine learning approach. Engineering Structures 2022;272:114918.
[38] Zheng M, Park CI, Liu X, Zhu R, Hu G, Kim YY. Non-resonant metasurface for broadband elastic wave mode splitting. Appl Phys Lett 2020;116:171903.
[39] Su X, Lu Z, Norris AN. Elastic metasurfaces for splitting sv-and p-waves in elastic solids. J Appl Phys 2018;123:091701.
[40] Liu Y, Liang Z, Liu F, Diba O, Lamb A, Li J. Source illusion devices for flexural lamb waves using elastic metasurfaces. Phys Rev Lett 2017;119:034301.
[41] Yang T, Lin Z, Zhu X, Yang T. Elastic metasurface with dual-coupled resonators for highly efficient energy harvesting. Phys Rev Appl 2022;18:064065.
[42] Lin Z, Tol S. Elastic metasurfaces for full wavefront control and low-frequency energy harvesting. Journal of Vibration and Acoustics 2021;143:
[43] Wen Z, Wang W, Khelif A, Djafari-Rouhani B, Jin Y. A perspective on elastic metastructures for energy harvesting. Appl Phys Lett 2022;120:020501.
[44] Zheng G, Mühlenbernd H, Kenney M, Li G, Zentgraf T, Zhang S. Metasurface holograms reaching 80% efficiency. Nature nanotechnology 2015;10:308-312.
[45] Kudyshev ZA, Kildishev AV, Shalaev VM, Boltasseva A. Machine-learning-assisted metasurface design for high-efficiency thermal emitter optimization. Applied Physics Reviews 2020;7:021407.
[46] Jia Y, Liu Y, Zhang W, Gong S. Ultra-wideband and high-efficiency polarization rotator

based on metasurface. Appl Phys Lett 2016;109:051901.
[47] Quan L, Alù A. Passive acoustic metasurface with unitary reflection based on nonlocality. Phys Rev Appl 2019;11:054077.
[48] Zhou H-T, Fu W-X, Wang Y-F, Wang Y-S. High-efficiency ultrathin nonlocal waterborne acoustic metasurface. Phys Rev Appl 2021;15:044046.
[49] Li J, Song A, Cummer SA. Bianisotropic acoustic metasurface for surface-wave-enhanced wavefront transformation. Phys Rev Appl 2020;14:044012.
[50] Li J, Shen C, Díaz-Rubio A, Tretyakov SA, Cummer SA. Systematic design and experimental demonstration of bianisotropic metasurfaces for scattering-free manipulation of acoustic wavefronts. Nat Commun 2018;9:1-9.
[51] Mei J, Wu Y. Controllable transmission and total reflection through an impedance-matched acoustic metasurface. New J Phys 2014;16:123007.
[52] Chen Y, Hu G. Broadband and high-transmission metasurface for converting underwater cylindrical waves to plane waves. Phys Rev Appl 2019;12:044046.
[53] Lee H, Lee JK, Seung HM, Kim YY. Mass-stiffness substructuring of an elastic metasurface for full transmission beam steering. J Mech Phys Solids 2018;112:577-593.
[54] Cao L, Yang Z, Xu Y, Assouar B. Deflecting flexural wave with high transmission by using pillared elastic metasurface. Smart Mater Struct 2018;27:075051.
[55] Jiang Y, Liu Y, Kou M, Li H, Wu X, Zeng X, et al. Multi-parameter independent manipulation for flexural wave by notched metasurface. Int J Mech Sci 2022;214:106928.
[56] Rong J, Ye W. Multifunctional elastic metasurface design with topology optimization. Acta Mater 2020;185:382-399.
[57] Su G, Du Z, Jiang P, Liu Y. High-efficiency wavefront manipulation in thin plates using elastic metasurfaces beyond the generalized snell's law. Mech Syst Signal Process 2022;179:109391.
[58] Minatti G, Caminita F, Martini E, Sabbadini M, Maci S. Synthesis of modulated-metasurface antennas with amplitude, phase, and polarization control. IEEE Trans Antennas Propag 2016;64:3907-3919.
[59] Yang Y, Jing L, Zheng B, Hao R, Yin W, Li E, et al. Full-polarization 3d metasurface cloak with preserved amplitude and phase. Adv Mater 2016;28:6866-6871.
[60] Zhu Y, Assouar B. Systematic design of multiplexed-acoustic-metasurface hologram with simultaneous amplitude and phase modulations. Phys Rev Mater 2019;3:045201.
[61] Fan S-W, Zhu Y, Cao L, Wang Y-F, Chen A-L, Merkel A, et al. Broadband tunable lossy metasurface with independent amplitude and phase modulations for acoustic holography. Smart Mater Struct 2020;29:105038.
[62] Su G, Zhang Y, Liu Y, Wang T. Steering flexural waves by amplitude-shift elastic metasurfaces. J Appl Mech 2021;88:
[63] Lin Z, Xu W, Wang W, Yuan S. Gradient folding metasurfaces with simultaneous phase

and amplitude modulation. J Mech Sci Technol 2021;35:5495-5501.
[64] Jiang M, Zhou H-T, Li X-S, Fu W-X, Wang Y-F, Wang Y-S. Extreme transmission of elastic metasurface for deep subwavelength focusing. Acta Mechanica Sinica 2022;38:1-10.
[65] Cao L, Yang Z, Xu Y, Chen Z, Zhu Y, Fan S-W, et al. Pillared elastic metasurface with constructive interference for flexural wave manipulation. Mechanical Systems and Signal Processing 2021;146:107035.
[66] Jin Y, Pennec Y, Djafari-Rouhani B. Acoustic analogue of electromagnetically induced transparency and autler–townes splitting in pillared metasurfaces. Journal of Physics D: Applied Physics 2018;51:494004.
[67] Zhu R, Qiu T, Wang J, Sui S, Li Y, Feng M, et al. Multiplexing the aperture of a metasurface: Inverse design via deep-learning-forward genetic algorithm. Journal of Physics D: Applied Physics 2020;53:455002.
[68] Wang Y, Zeng Q, Wang J, Li Y, Fang D. Inverse design of shell-based mechanical metamaterial with customized loading curves based on machine learning and genetic algorithm. Computer Methods in Applied Mechanics and Engineering 2022;401:115571.
[69] Chang Y, Wang H, Dong Q. Machine learning-based inverse design of auxetic metamaterial with zero poisson's ratio. Materials Today Communications 2022;30:103186.
[70] Chipperfield A, Fleming P. The matlab genetic algorithm toolbox. 1995;
[71] Sivanandam S, Deepa S Genetic algorithm implementation using matlab. in: Introduction to genetic algorithms, Springer, 2008, pp. 211-262.
[72] Kumar M, Husain D, Upreti N, Gupta D. Genetic algorithm: Review and application. Available at SSRN 3529843 2010;
[73] Hashim AA, Mahmoud KI, Ridha HM. Geometry and shape optimization of piezoelectric cantilever energy harvester using comsol multiphysics software. International Review of Applied Sciences and Engineering 2021;12:103-110.
[74] Ozana S, Pies M, Hajovsky R Using matlab and comsol multiphysics for optimization of the model of underground thermal processes at old mining dumps. in: Applied Mechanics and Materials, Trans Tech Publ, 2014, pp. 571-578.
[75] Muñoz JS, Valencia R, Nieto C Comsol and matlab® integration to optimize heat exchangers using genetic algorithms technique. in: Proceedings of the COMSOL Conference, 2008.
[76] Konstantinidis K, Feresidis AP, Hall PS. Multilayer partially reflective surfaces for broadband fabry-perot cavity antennas. IEEE Trans Antennas Propag 2014;62:3474-3481.

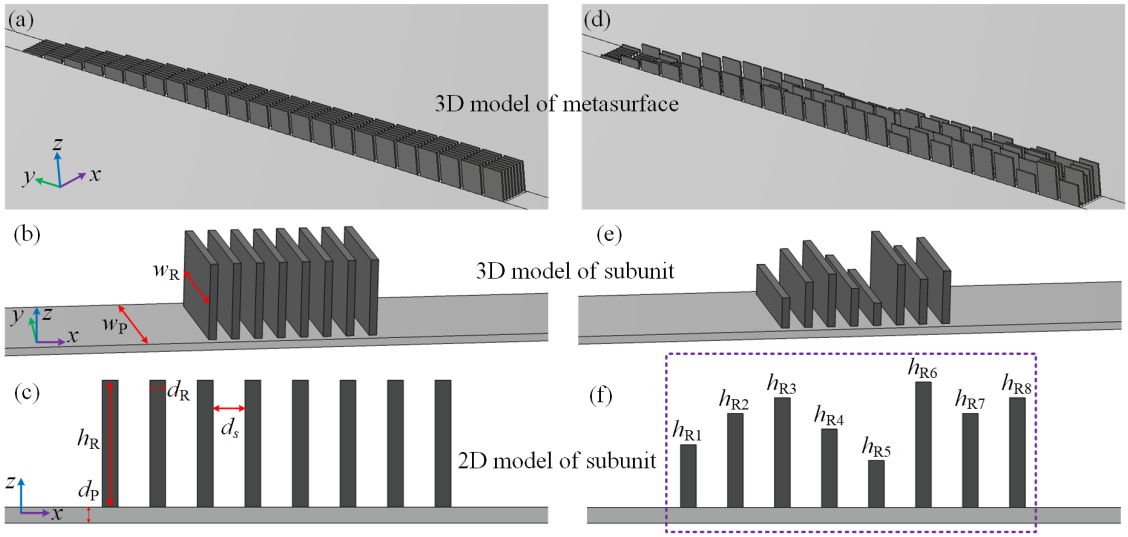

Fig. 1. (a) Schematic 3D model of the pillared elastic metasurface, (b) schematic 3D model of the subunit, (c) schematic 2D model (plane strain model) of the subunit for the periodic design. (d) Schematic 3D model of the pillared elastic metasurface, (e) schematic 3D model of the subunit, (f) schematic 2D model (plane strain model) of the subunit for the aperiodic design.

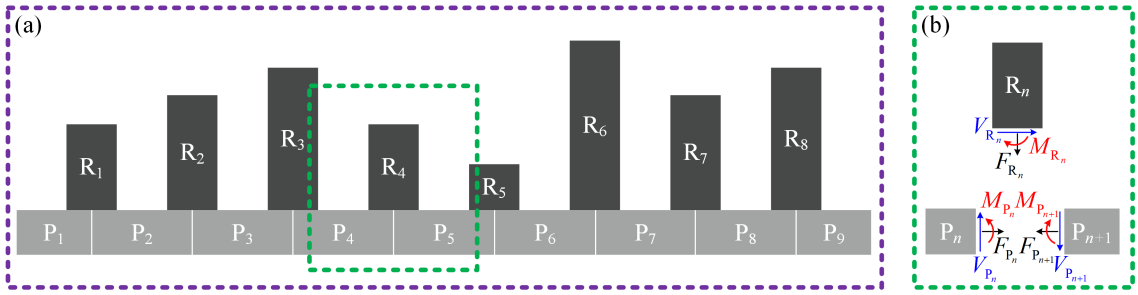

Fig. 2. (a) Sketch showing that the subunit is divided into several regions. (b) Sketch of the unit cell composed of the *n*th host plate region (P_n), the (*n*+1)th host plate region (P_{n+1}) and the *n*th pillared resonator (R_n).

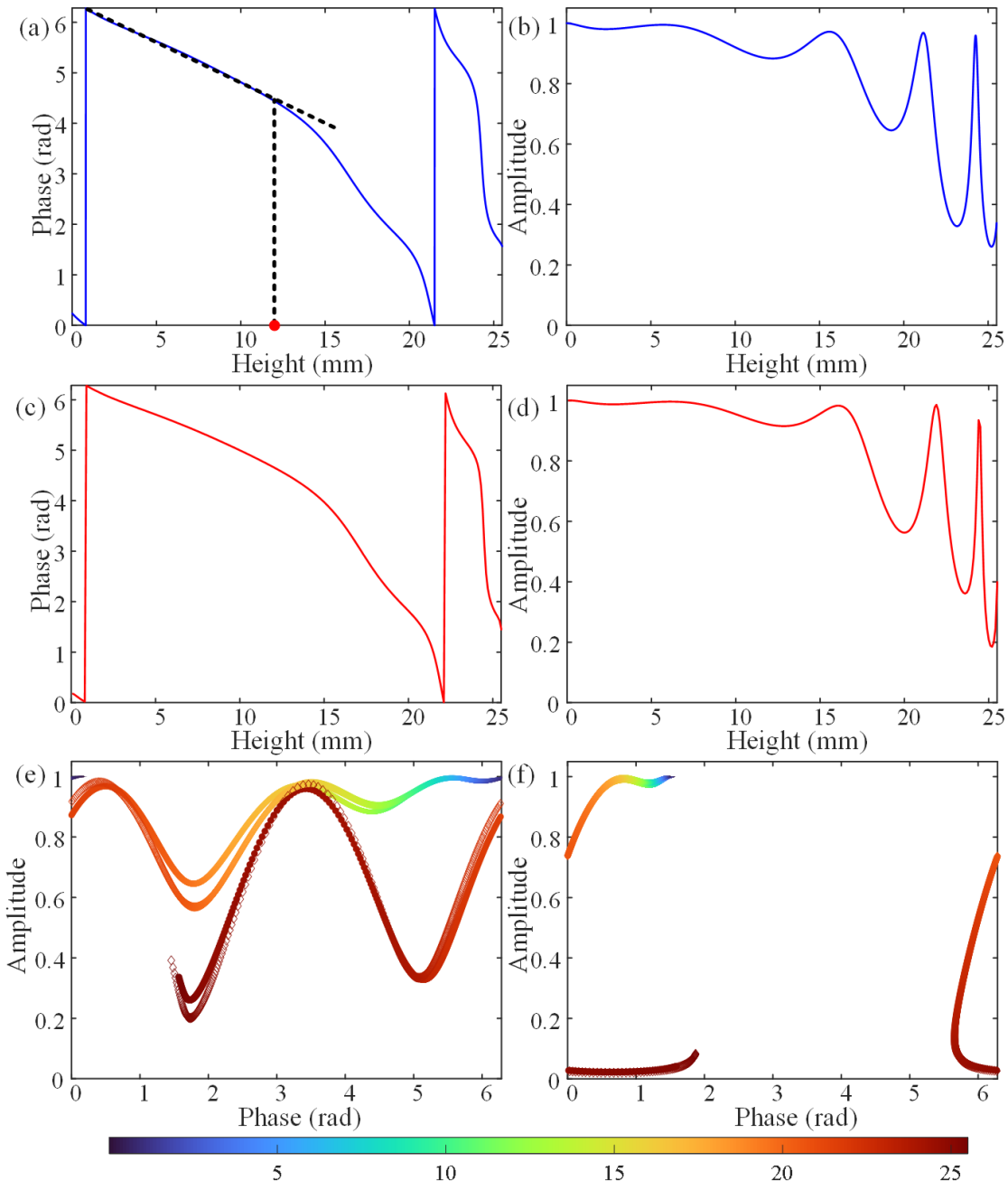

Fig. 3. (a) Phase and (b) amplitude obtained from the analytical model. (c) Phase and (d) amplitude obtained from the 3D FEM. The relationship between phase and amplitude at different pillared resonator heights for the subunit with (e) 8 pillared resonators and (f) 1 pillared resonator.

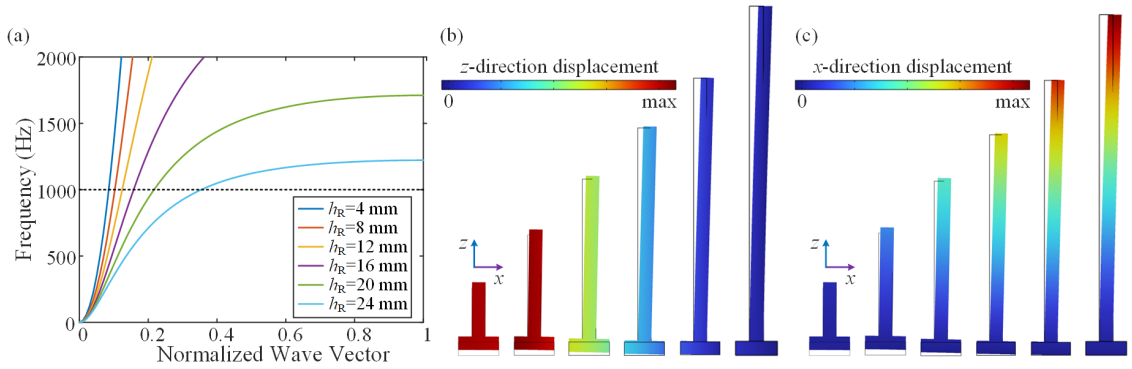

Fig. 4. (a) The lowest dispersion bands for the unit cells with different heights. (b)-(c) Vibration modes of the pillared resonators with different heights.

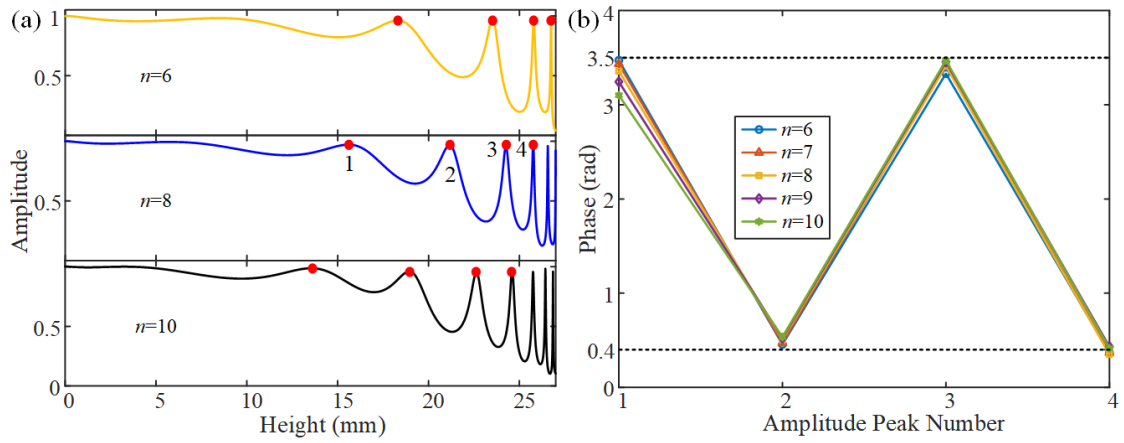

Fig. 5. (a) Amplitude curve of the subunit with different number of pillared resonators. (b) Phases at the peak points in the amplitude curve with different number of pillared resonators.

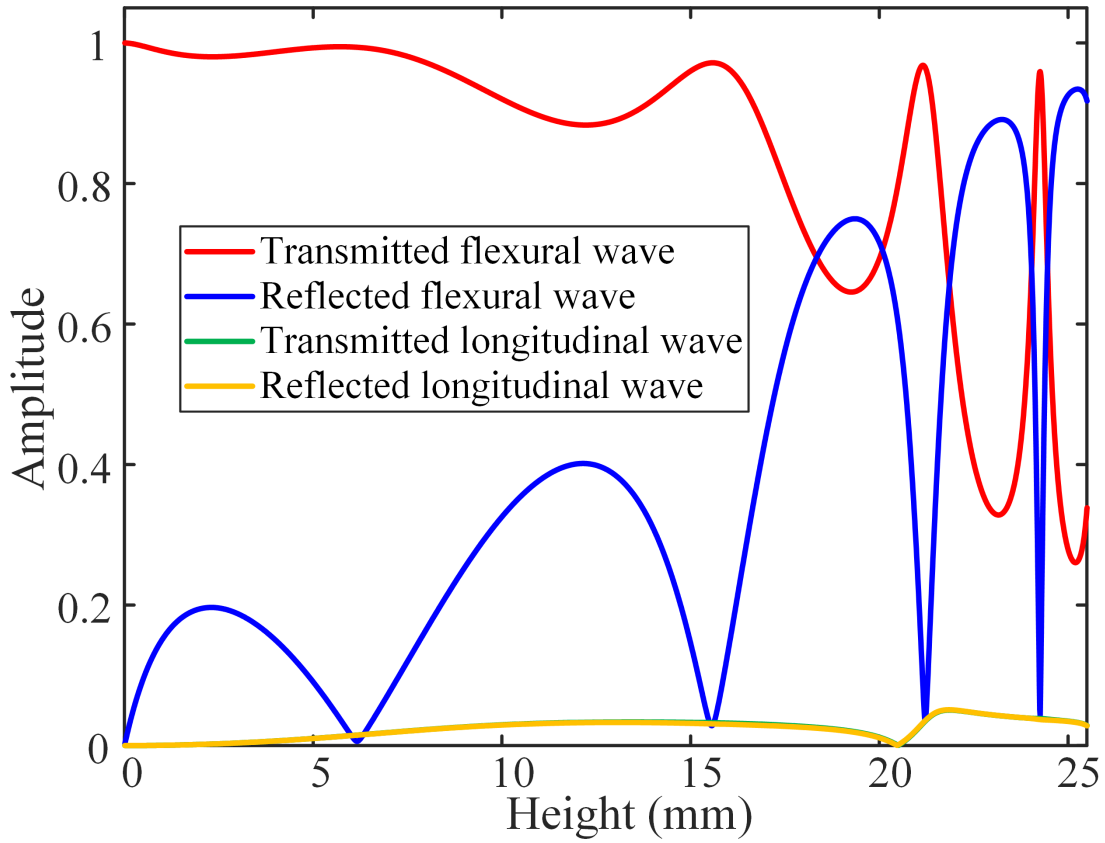

Fig. 6. Amplitude of the transmitted flexural wave, reflected flexural wave, transmitted longitudinal wave, and reflected longitudinal wave at different heights.

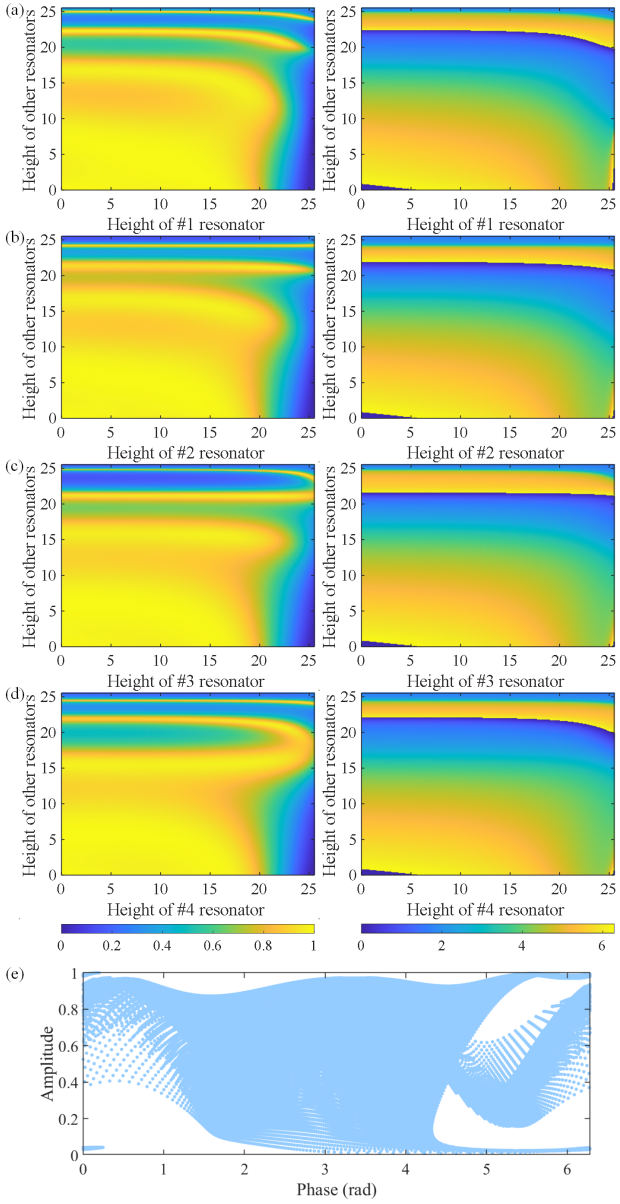

Fig. 7. The range of amplitude (left) and phase (right) when the height of the (a) 1st, (b) 2nd, (c) 3rd, and (d) 4th pillared resonator is different from the other pillared resonators. (e) The combination range between phase and amplitude when only one pillared resonator has different height.

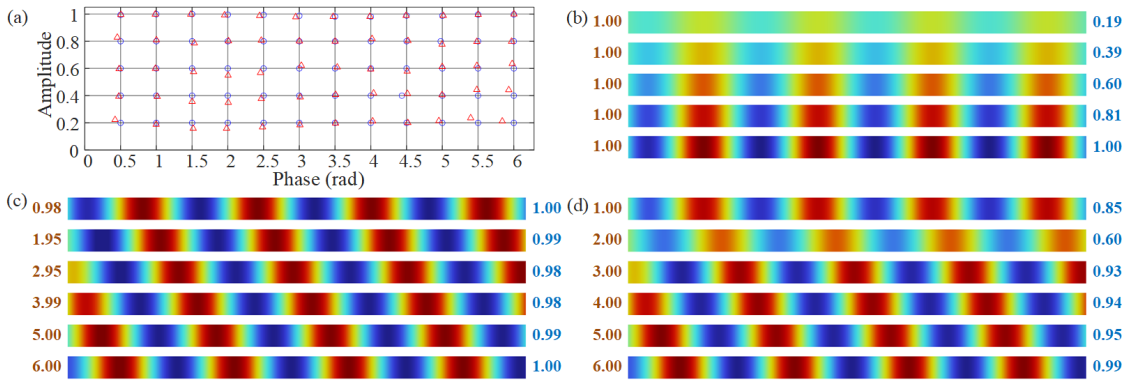

Fig. 8. (a) The results of the combination between phase and amplitude. The blue circles represent the analytical results and the red triangles represent the corresponding FEM results. (b) Out-of-plane displacement distribution of the transmitted wave field for the subunit with the same phase (1 rad) but different amplitudes (an interval of 0.2) of the aperiodic design. (c) Out-of-plane displacement distribution of the transmitted wave field for the subunit with the different phases (an interval of 1 rad) but same amplitude (1) of the aperiodic design. (d) Out-of-plane displacement distribution of the transmitted wave field for the subunit with different phases (an interval of 1 rad) of the periodic design. (The left brown numbers mean the phase and the right blue numbers mean the amplitude obtained from the FEM.)

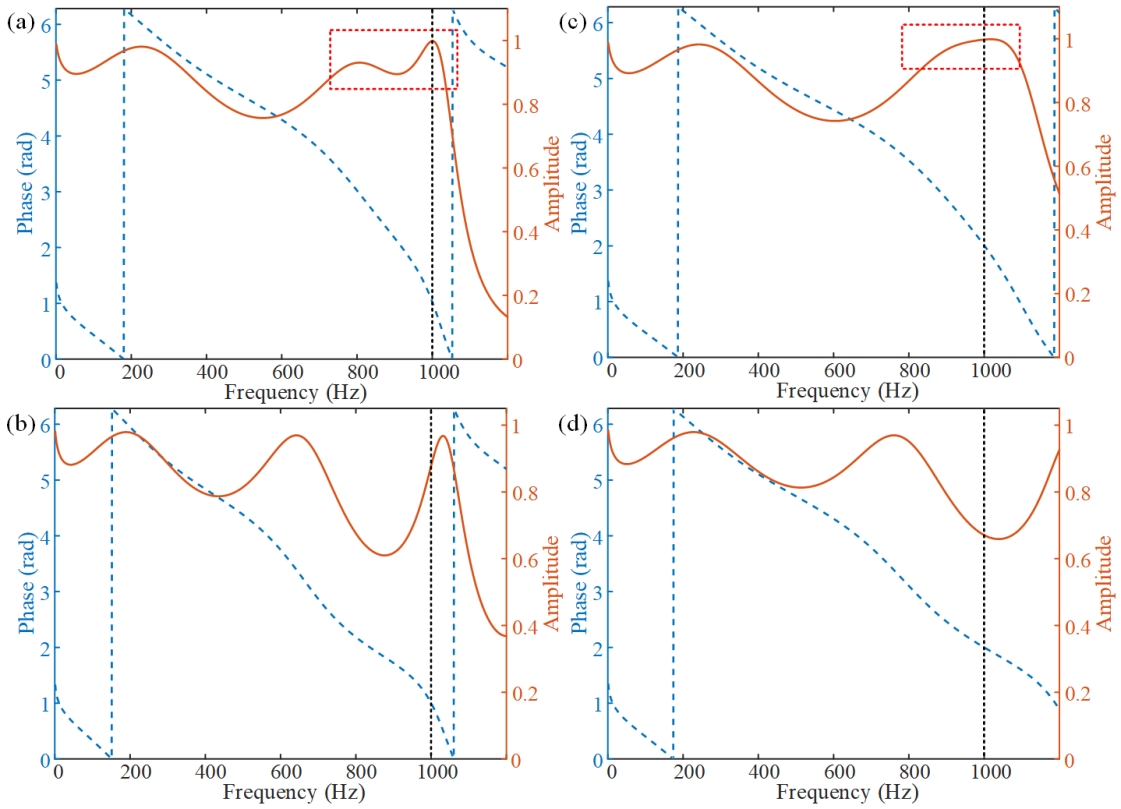

Fig. 9. The curve of amplitude and phase at different frequencies when the phase is 1 rad for the (a) aperiodic and (b) periodic design. The curve of amplitude and phase at different frequencies when the phase is 2 rad for the (c) aperiodic and (d) periodic design.

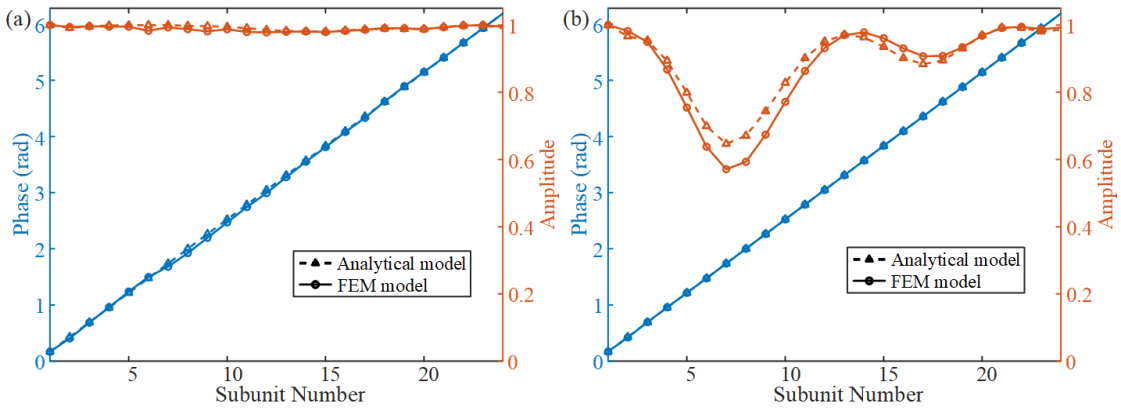

Fig. 10. Phase and amplitude of the subunit in the (a) aperiodic and (b) periodic deign to steer flexural waves into one direction with full transmission.

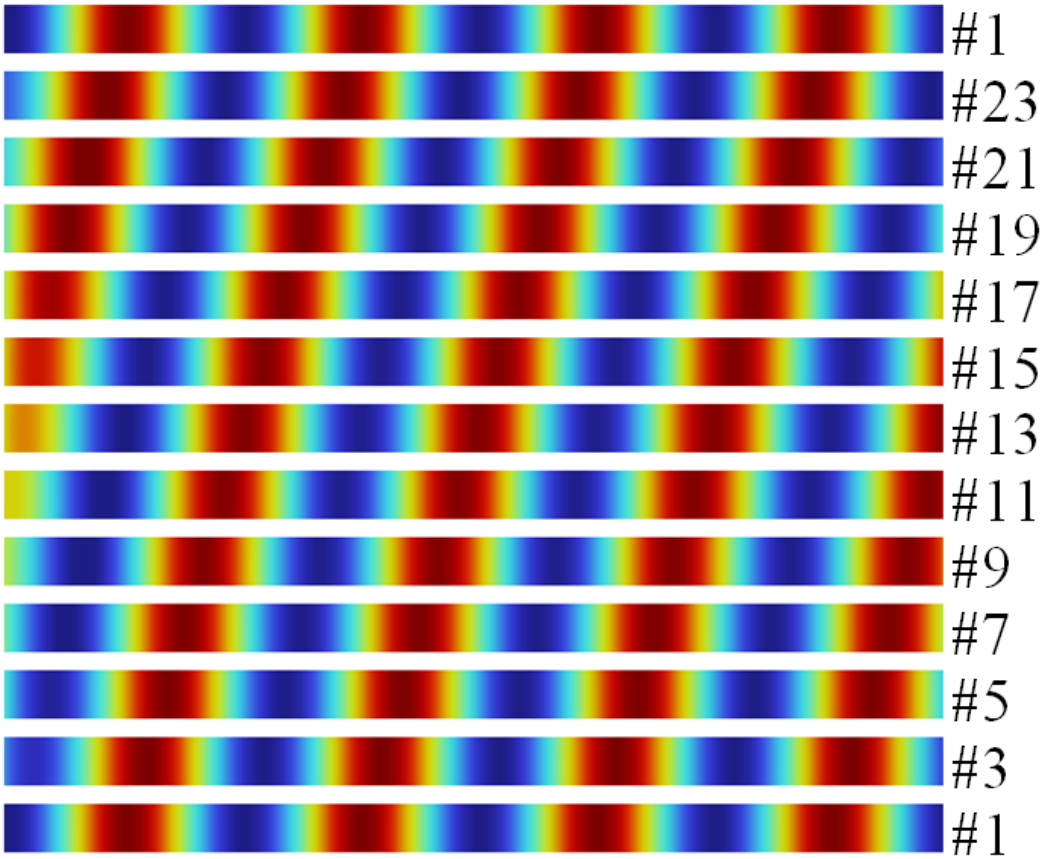

Fig. 11. Out-of-plane displacement distribution of the transmitted wave field in the subunit with a $\frac{\pi}{6}$ phase interval.

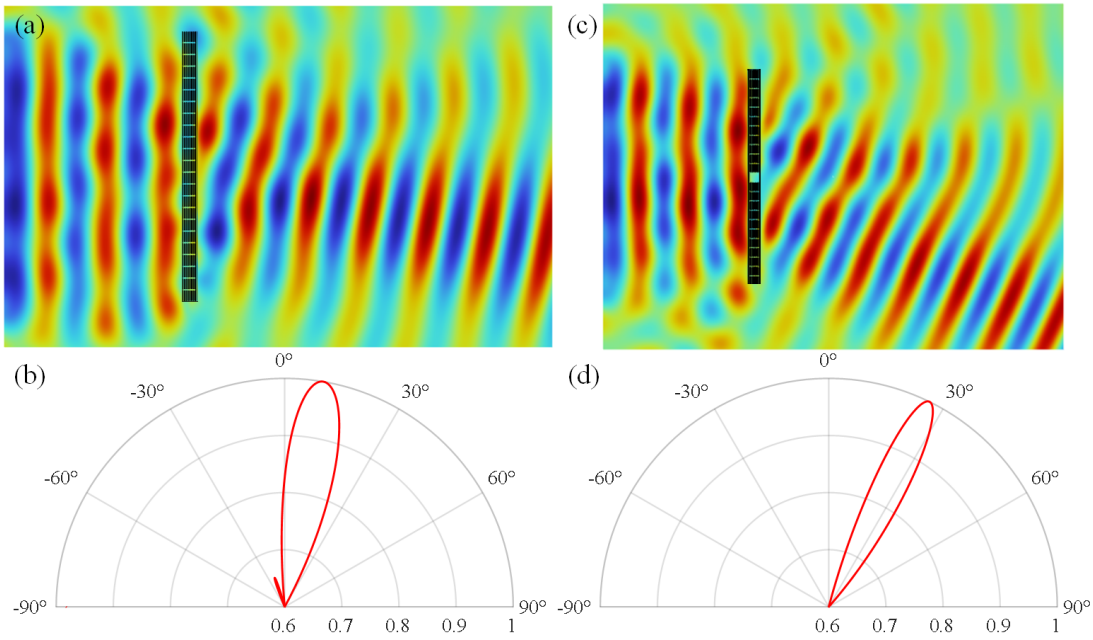

Fig. 12. The numerical simulation results of the out-of-plane displacement distribution for the metasurface to steer waves into one direction with full transmission when the refraction angle is (a) 12.02° and (c) 24.62°. Polar directivity graphs of the transmitted waves measured at three wavelengths away from the center of the metasurface to steer waves into one direction with full transmission when the refraction angle is (b) 12.02° and (d) 24.62°.

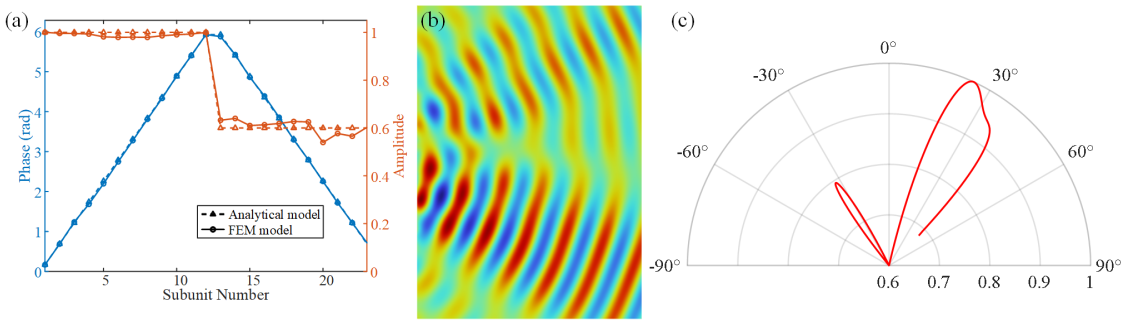

Fig. 13. (a) Phase and amplitude of the subunit. (b) The numerical simulation results of the out-of-plane displacement distribution. (c) Polar directivity graphs of the transmitted waves measured at three wavelengths away from the center of the metasurface to steer waves into two directions with different amplitudes.

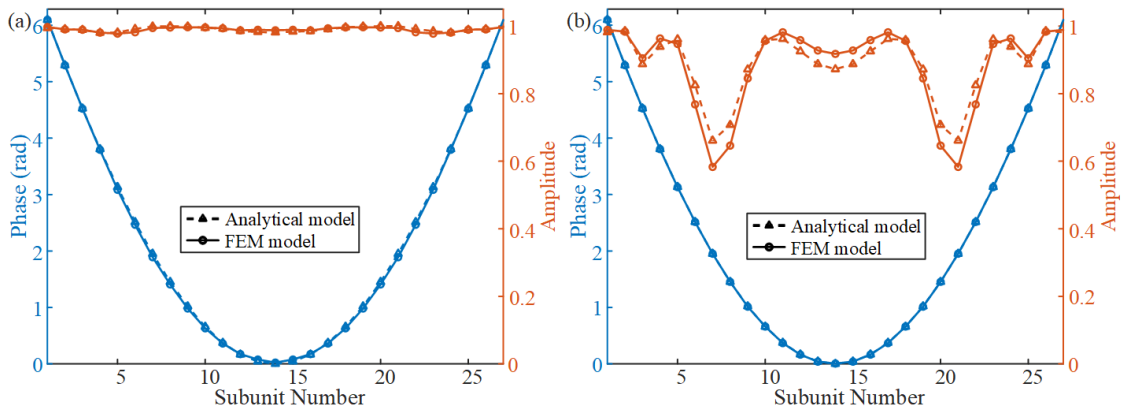

Fig. 14. Phase and amplitude of the subunit in the (a) aperiodic and (b) periodic deign to focus flexural waves.

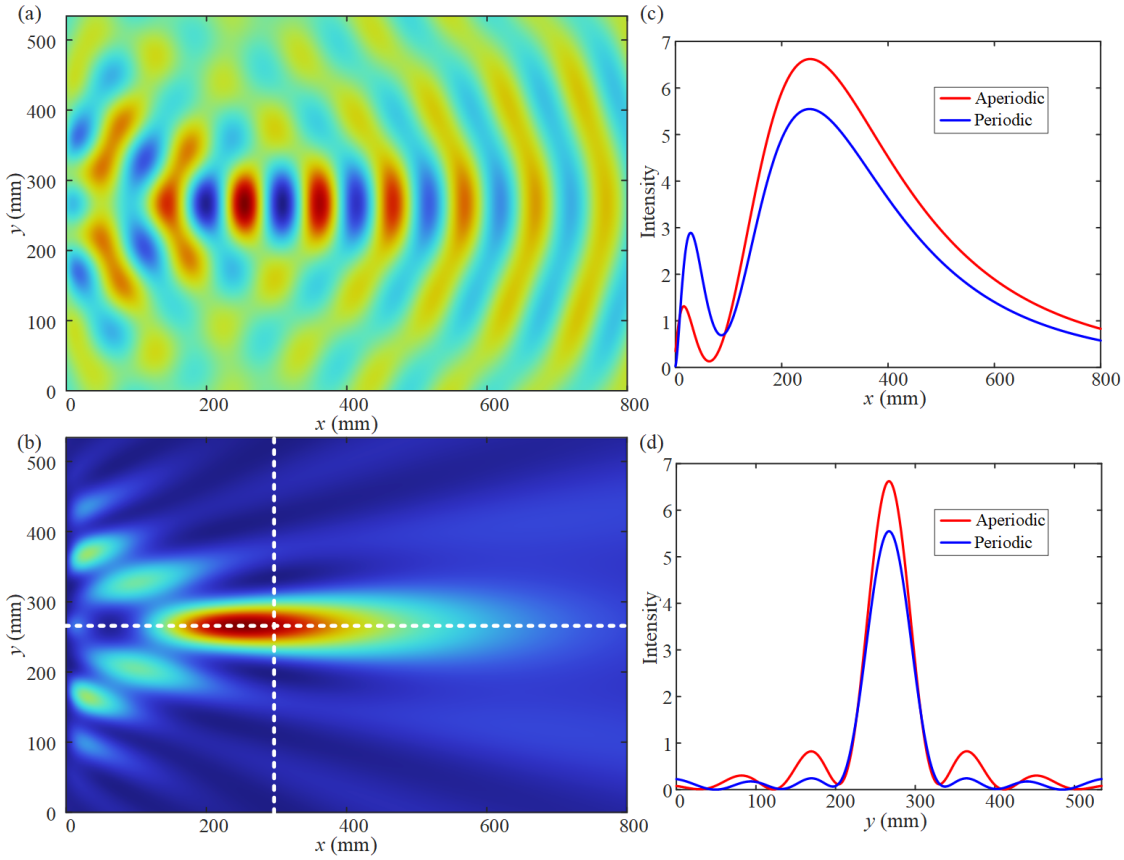

Fig. 15. The numerical simulation results of the (a) out-of-plane displacement distribution and (b) the normalized energy intensity distribution for the metasurface to focus waves with full transmission. Normalized energy intensity distribution along the (c) transverse and (d) vertical direction of the white dashed line.

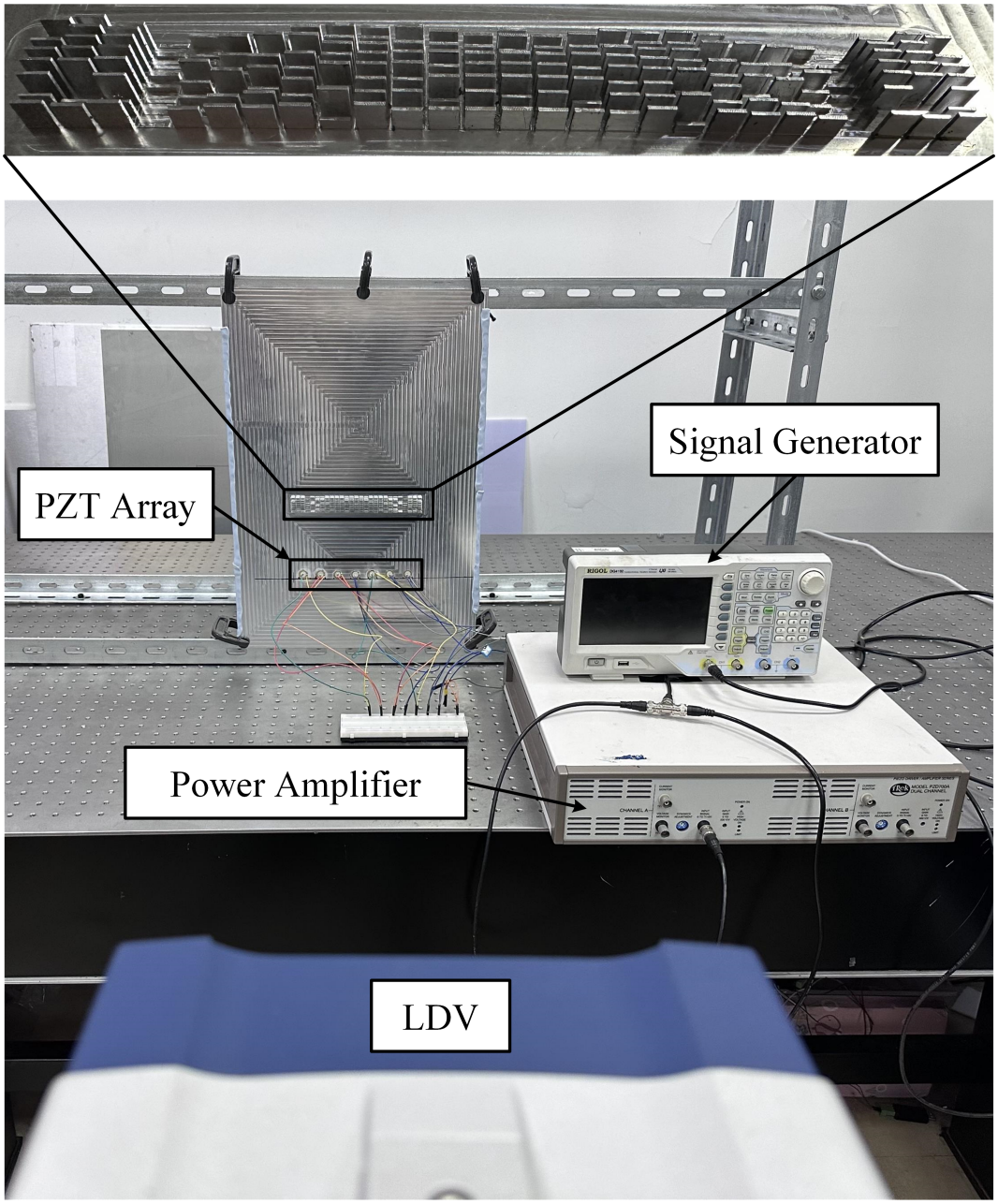

Fig. 16. Photo of the experimental setup.

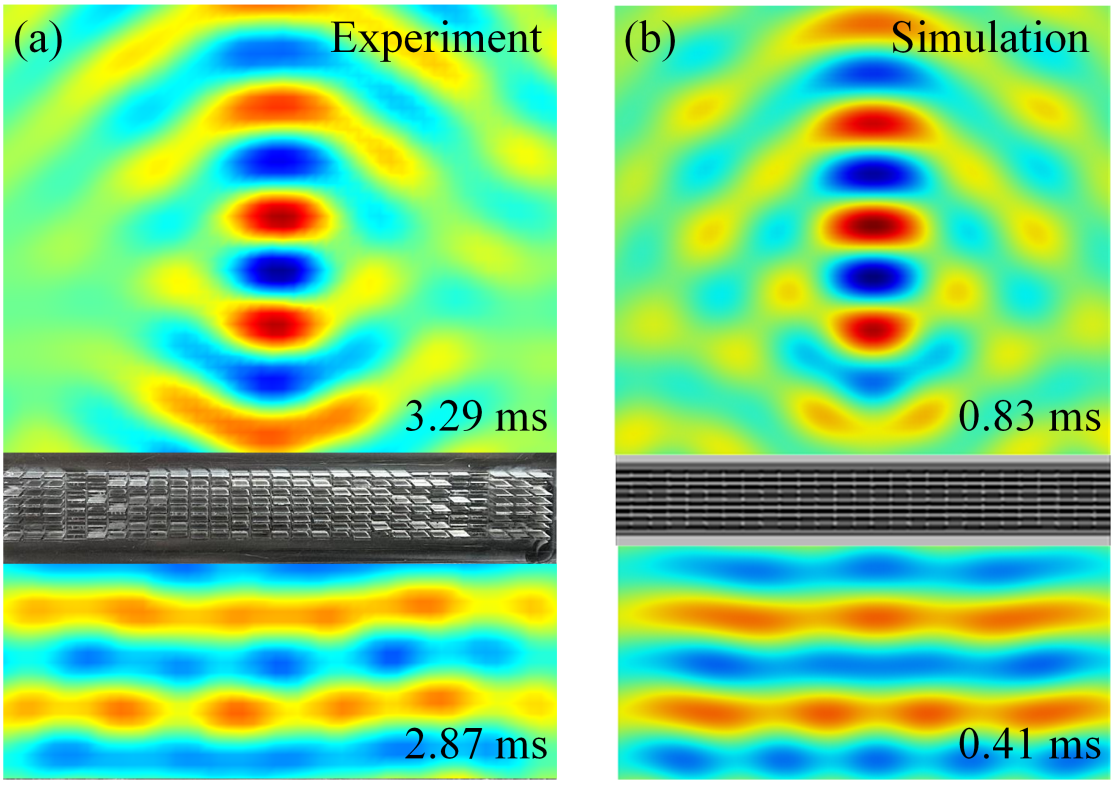

Fig. 17. Distribution of the out-of-plane velocity in the host plate obtained from (a) experiment and (b) simulation.